INTERNATIONAL JOURNAL FOR NUMERICAL METHODS IN FLUIDS
Int. J. Numer. Meth. Fluids 2001; **36**: 465–496 (DOI: 10.1002/fld.146)

Simulation of non-linear free surface motions in a cylindrical domain using a Chebyshev–Fourier spectral collocation method

M. J. Chern, A. G. L. Borthwick* and R. Eatock Taylor

Department of Engineering Science, University of Oxford, Parks Road, Oxford, U.K.

SUMMARY

When a liquid is perturbed, its free surface may experience highly non-linear motions in response. This paper presents a numerical model of the three-dimensional hydrodynamics of an inviscid liquid with a free surface. The mathematical model is based on potential theory in cylindrical co-ordinates with a σ-transformation applied between the bed and free surface in the vertical direction. Chebyshev spectral elements discretize space in the vertical and radial directions; Fourier spectral elements are used in the angular direction. Higher derivatives are approximated using a collocation (or pseudo-spectral) matrix method. The numerical scheme is validated for non-linear transient sloshing waves in a cylindrical tank containing a circular surface-piercing cylinder at its centre. Excellent agreement is obtained with Ma and Wu's [Second order transient waves around a vertical cylinder in a tank. *Journal of Hydrodynamics* 1995; **Ser. B4**: 72–81] second-order potential theory. Further evidence for the capability of the scheme to predict complicated three-dimensional, and highly non-linear, free surface motions is given by the evolution of an impulse wave in a cylindrical tank and in an open domain. Copyright © 2001 John Wiley & Sons, Ltd.

KEY WORDS: non-linear free surface motions; spectral collocation method; σ-transformation

1. INTRODUCTION

Analysis of non-linear free surface motions of liquids with low viscosity is extremely important in a number of engineering contexts. Extreme ocean waves can be sufficiently steep for their front face to cause resonant ringing-type responses of offshore structures. For example, storm waves measured at the Tern platform in the northern North Sea were found to be non-linear in profile with the peak crest elevation 25.5 m above mean water level [1]. Sloshing motions occur when tanks containing liquids with a free surface are disturbed. Solitary waves may arise as tsunami from earthquake, volcanic or meteoric disturbances. The classical dam break problem is another example of a transient free surface flow.

* Correspondence to: Department of Engineering Science, University of Oxford, Parks Road, Oxford OX1 3PJ, U.K.

Received July 1999
Revised January 2000

For inviscid liquids, the fluid motion is governed by Laplace's equation for the velocity potential, subject to non-linear dynamic and kinematic free surface boundary conditions. Analytical solutions are restricted to certain idealized cases for simple geometries. For example, Stokes [2] derived perturbation expansions to describe regular progressive waves of finite amplitude passing over a flat bed. Schwarz [3] and Fenton [4] obtained solutions of Stokes' expansions to fifth order and above. A third-order analytical solution in the frequency domain has been determined by Malenica and Molin [5] for wave diffraction by a vertical cylinder. Ma and Wu [6] developed a second-order solution for the case of transient sloshing waves in a circular tank containing a vertical cylinder at its centre.

Since Yeung's [7] review of numerical methods for predicting free surface flows, the subject has undergone major expansion. For example, advances have occurred regarding the accurate prediction of inviscid free surface transients using boundary integral element (e.g. Dold and Peregrine [8], Wang *et al.* [9], Ferrant [10]), Fourier series (e.g. Taylor and Haagsma [11], Johannessen [12]), polynomial series (Fenton [13]), kinematic boundary condition fitting (Forristal [14]), finite difference (e.g. Yeung and Vaidhanathan [15]), and finite element methods (e.g. Wu and Eatock Taylor [16]). These models have been applied to steep nearly overturning waves in flumes, extreme waves in directional seas, focused unidirectional waves, solitons, tank sloshing, etc. Some can cope with immersed bodies (e.g. Wu and Eatock Taylor's finite element approach) whereas others have been designed for waves in the absence of internal obstacles (e.g. Johannessen [12]). As yet, there is no consensus regarding which technique is best for a given situation. For example, Ma and Wu [6] argue that finite elements may be more efficient than boundary elements for non-linear wave modelling even though finite elements involve discretization of the entire flow field. Viscous free surface flows have also been considered. Yu and Yeung [17] used a pseudo-spectral scheme to solve the Navier–Stokes equations with linearized boundary conditions for free surface motions in a cylindrical container with a central cylinder.

The spectral element method is a computationally efficient alternative to finite element or finite difference methods (the efficiency being related to the numbers of mesh nodes required to achieve a solution to a given accuracy). Originally devised by meteorologists, the spectral method was first subjected to a rigorous mathematical assessment in the monograph by Gottlieb and Orszag [18]. Hussaini and Zang [19] and Canuto *et al.* [20] have produced comprehensive reviews of spectral element applications in computational fluid dynamics. In a recent paper, the present authors [21] applied the collocation (or pseudo-spectral) matrix method to solve the sigma-transformed potential flow equations in two-dimensional Cartesian form. Two-dimensional non-linear free surface sloshing in a rectangular tank was simulated, and close agreement with Wu and Eatock Taylor's [16] second-order analytical solution was obtained.

In this paper, details are given of a pseudo-spectral numerical scheme for modelling the three-dimensional free surface motions of a perturbed inviscid liquid. The mathematical formulation is based on fully non-linear potential theory expressed in a σ-transformed cylindrical co-ordinate system mapped onto a rectangular box. Chebyshev (radial and vertical directions) and Fourier (angular direction) collocated points form a grid within the box. The potential flow equations are discretized using Chebyshev and Fourier pseudo-spectral matrix techniques. The scheme provides a detailed picture of fully non-linear free surface motions,

provided that the liquid is continuous between the free surface and bed in the vertical direction. Results are presented for axisymmetric sloshing motions in a cylindrical tank containing a central vertical cylinder, and for asymmetric free surface patterns caused by an off-centre surface perturbation in the same tank and in an open domain.

2. MATHEMATICAL MODEL OF FREE SURFACE WAVES IN A CYLINDRICAL DOMAIN

It is assumed that the fluid is incompressible, inviscid and hence irrotational. In a cylindrical system, the governing equation for mass conservation may be expressed in terms of velocity potential ϕ as

$$\frac{\partial^2\phi}{\partial r^2}+\frac{1}{r}\frac{\partial\phi}{\partial r}+\frac{1}{r^2}\frac{\partial^2\phi}{\partial\theta^2}+\frac{\partial^2\phi}{\partial z^2}=0 \tag{1}$$

where r, θ and z refer to the radial, tangential and azimuthal co-ordinates.

At the gas–liquid interface, the non-linear dynamic and kinematic free surface boundary conditions are respectively

$$\frac{\partial\phi}{\partial t}+g\eta+\frac{1}{2}(u_r^2+u_\theta^2+u_z^2)=0 \quad \text{at } z=\eta \tag{2}$$

and

$$\frac{\partial\eta}{\partial t}=\frac{\partial\phi}{\partial z}-\frac{\partial\phi}{\partial r}\frac{\partial\eta}{\partial r}-\frac{1}{r^2}\frac{\partial\phi}{\partial\theta}\frac{\partial\eta}{\partial\theta} \quad \text{at } z=\eta \tag{3}$$

where the velocity components are

$$u_r=\frac{\partial\phi}{\partial r}, \qquad u_\theta=\frac{1}{r}\frac{\partial\phi}{\partial\theta}, \qquad u_z=\frac{\partial\phi}{\partial z} \tag{4}$$

In Equation (2), which is derived from the modified Bernoulli equation applied on the free surface, it is presumed that atmospheric pressure relative to the gas-liquid boundary is zero.

There is no flow through the bed, and so the bottom boundary condition is

$$\frac{\partial\phi}{\partial z}=0 \quad \text{at } z=-d \tag{5}$$

where d is the still water depth.

Similarly, there is no flow through the solid walls of an inner cylinder of radius r_I located at the centre of the domain, and so

$$\frac{\partial \phi}{\partial r} = 0 \quad \text{at } r = r_{\mathrm{I}} \tag{6}$$

For a cylindrical tank domain with an outer solid wall perimeter

$$\frac{\partial \phi}{\partial r} = 0 \quad \text{at } r = r_{\mathrm{O}} \tag{7}$$

where r_{O} is the radius of the cylindrical tank.

For a cylindrical domain with open perimeter, a Sommerfeld radiation condition is applied (see, for example, Orlanski [22], Chan [23], Romate [24], Broeze and Romate [25]), and is expressed in cylindrical co-ordinates by

$$\frac{\partial \phi}{\partial t} + c\frac{\partial \phi}{\partial r} = 0 \tag{8}$$

which can be asymptotically satisfied by a linear propagating wave. In this case, c is the phase velocity of the wave, which is a function of the wave frequency, and is often formulated as $(gh)^{1/2}$ in shallow water.

The pressure distribution on the surface of the inner cylinder is given by the modified Bernoulli equation as

$$p = -\rho g z - \frac{\rho}{2}(u_\theta^2 + u_z^2) - \rho\frac{\partial \phi}{\partial t} \tag{9}$$

where p is pressure and ρ is fluid density. Hence, the horizontal force components acting on the inner cylinder are

$$F_x = -\int_{-d}^{\eta}\int_0^{2\pi} p\cos\theta r_{\mathrm{I}}\,\mathrm{d}\theta\,\mathrm{d}z \quad \text{and} \quad F_y = -\int_{-d}^{\eta}\int_0^{2\pi} p\sin\theta r_{\mathrm{I}}\,\mathrm{d}\theta\,\mathrm{d}z \tag{10}$$

The three-dimensional governing equation and boundary conditions are transformed from a cylindrical co-ordinate system where r, θ, $z \in [r_{\mathrm{I}}, r_{\mathrm{O}}] \times [0, 2\pi] \times [-d, \eta]$, to a rectangular box system, where R, θ, $\sigma \in [-1, 1] \times [0, 2\pi] \times [-1, 1]$, by applying algebraic stretch transformations in the radial and azimuthal directions. The radial transformation consists of a simple linear stretch expressed as

$$R(r) = -1 + \frac{2(r - r_{\mathrm{I}})}{b} \tag{11}$$

where b is $r_{\mathrm{O}} - r_{\mathrm{I}}$. In the z-direction, a linear σ-transform is used, such that

$$\sigma(r, \theta, t) = -1 + \frac{2(z + d)}{h} \tag{12}$$

where d is the still water depth and h is the total depth ($h = d + \eta$). The σ-transform is easier to implement than a general curvilinear co-ordinate transformation, but has the constraint that the mapping has to be unique, and so it cannot deal with overturning waves or spray formation.

The above transformations map the velocity potential $\phi(r, \theta, z, t)$ in the physical domain onto $\Phi(R, \theta, \sigma, t)$. After applying the chain rule and rearranging, the transformed governing equation may be written:

$$\frac{1}{b^2}\frac{\partial^2\Phi}{\partial R^2}+\frac{1}{qb}\frac{\partial\Phi}{\partial R}+\frac{1}{q^2}\frac{\partial^2\Phi}{\partial\theta^2}+\left[\frac{1}{b^2h}\left(\frac{\partial\alpha}{\partial R}-2\frac{\alpha}{h}\frac{\partial\eta}{\partial R}\right)+\frac{1}{qb}\frac{\alpha}{h}+\frac{1}{q^2h}\left(\frac{\partial\beta}{\partial\theta}-2\frac{\beta}{h}\frac{\partial\eta}{\partial\theta}\right)\right]\frac{\partial\Phi}{\partial\sigma}$$
$$+2\frac{\alpha}{b^2h}\frac{\partial^2\Phi}{\partial R\,\partial\sigma}+2\frac{\beta}{q^2h}\frac{\partial^2\Phi}{\partial\theta\,\partial\sigma}+\left[\left(\frac{\alpha}{bh}\right)^2+\left(\frac{\beta}{qh}\right)^2+\frac{1}{h^2}\right]\frac{\partial^2\Phi}{\partial\sigma^2}=0 \tag{13a}$$

where

$$q = b(R+1)+2r_1 \tag{13b}$$

$$\alpha = -(\sigma+1)\frac{\partial\eta}{\partial R}, \qquad \beta = -(\sigma+1)\frac{\partial\eta}{\partial\theta} \tag{13c}$$

$$\frac{\partial\alpha}{\partial R} = -(\sigma+1)\frac{\partial^2\eta}{\partial R^2} \quad \text{and} \quad \frac{\partial\beta}{\partial\theta} = -(\sigma+1)\frac{\partial^2\eta}{\partial\theta^2} \tag{13d}$$

The transformed dynamic free surface boundary condition is

$$\frac{\partial\Phi}{\partial t}+\frac{\gamma}{h}\frac{\partial\Phi}{\partial\sigma}+g\eta+\frac{2}{b^2}\left(\frac{\partial\Phi}{\partial R}+\frac{\alpha}{h}\frac{\partial\Phi}{\partial\sigma}\right)^2+\frac{2}{q^2}\left(\frac{\partial\Phi}{\partial\theta}+\frac{\beta}{h}\frac{\partial\Phi}{\partial\sigma}\right)^2+\frac{2}{h^2}\left(\frac{\partial\Phi}{\partial\sigma}\right)^2 \quad \text{at } \sigma=1 \tag{14a}$$

where

$$\gamma = -(\sigma+1)\frac{\partial\eta}{\partial t} \tag{14b}$$

The transformed kinematic free surface boundary condition and bed boundary conditions are

$$\frac{\partial\eta}{\partial t}=\left(\frac{2}{h}-\frac{4\alpha}{b^2h}-\frac{4\beta}{q^2h}\frac{\partial\eta}{\partial\theta}\right)\frac{\partial\Phi}{\partial\sigma}-\frac{4}{b^2}\frac{\partial\Phi}{\partial R}\frac{\partial\eta}{\partial R}-\frac{4}{q^2}\frac{\partial\Phi}{\partial\theta}\frac{\partial\eta}{\partial\theta} \quad \text{at } \sigma=1 \tag{15}$$

and

$$\frac{\partial\Phi}{\partial\sigma}=0 \quad \text{at } \sigma=-1 \tag{16}$$

At solid cylindrical walls, the transformed no flow boundary condition is

$$\frac{\partial \Phi}{\partial R} + \frac{\alpha}{h}\frac{\partial \Phi}{\partial \sigma} = 0 \quad \text{at } R = -1 \quad \text{and} \quad R = 1 \tag{17}$$

For a far field open boundary, the transformed Sommerfeld boundary condition is

$$\frac{\partial \Phi}{\partial t} = -\frac{\gamma}{h}\frac{\partial \Phi}{\partial \sigma} - c\left[\frac{\partial \Phi}{\partial R} + \frac{\alpha}{h}\frac{\partial \Phi}{\partial \sigma}\right] \tag{18}$$

where c is the phase velocity of the linear wave.

In conjunction with an initial free surface profile, Equations (13)–(18) constitute the mathematical model for three-dimensional transient free surface motions of inviscid liquid in a cylindrical domain. The pressure on the surface of the inner cylinder in the transformed system is:

$$p(r, \theta, \sigma, t) = -pg\left[\frac{h(\sigma+1)}{2} - d\right] - \frac{\rho}{2}\left[\frac{4}{q^2}\left(\frac{\partial \Phi}{\partial \theta} + \frac{\beta}{h}\frac{\partial \Phi}{\partial \sigma}\right)^2 + \frac{4}{h^2}\left(\frac{\partial \Phi}{\partial \sigma}\right)^2\right] - \rho\frac{\partial \Phi}{\partial t} - \rho\frac{\gamma}{h}\frac{\partial \Phi}{\partial \sigma} \tag{19}$$

The horizontal force components acting on the inner cylinder are therefore

$$F_x = -\frac{1}{2}\int_{-1}^{1}\int_{0}^{2\pi} hp\cos\theta r_{\mathrm{I}}\,\mathrm{d}\theta\,\mathrm{d}\sigma \quad \text{and} \quad F_y = -\frac{1}{2}\int_{-1}^{1}\int_{0}^{2\pi} hp\sin\theta r_{\mathrm{I}}\,\mathrm{d}\theta\,\mathrm{d}\sigma \tag{20}$$

3. NUMERICAL SCHEME

The transformed domain consists of a rectangular box, which is discretized according to Chebyshev and Fourier collocation formulae as follows:

$$R_i = \cos\left(\frac{i\pi}{M}\right), \quad \theta_j = \frac{2j\pi}{N} \quad \text{and} \quad \sigma_k = \cos\left(\frac{k\pi}{L}\right) \tag{21}$$

for $i = 0, 1, \ldots, M$, $j = 0, 1, \ldots, N-1$, and $k = 0, 1, \ldots, L$. Note that the indexing system used here works in the reverse R and σ directions. For example, $i = 0$ refers to $R = -1$. The physical grid system is shown in Figure 1. Chebyshev spectral elements are used to discretize space in the vertical and radial directions, leading to element concentration near the cylindrical boundaries. Fourier spectral elements are used in the angular direction where uniform element spacing is desirable.

The third-order Adams–Bashforth (AB3) scheme is used for all time-integrations, whereby the updated value of a variable f is given by

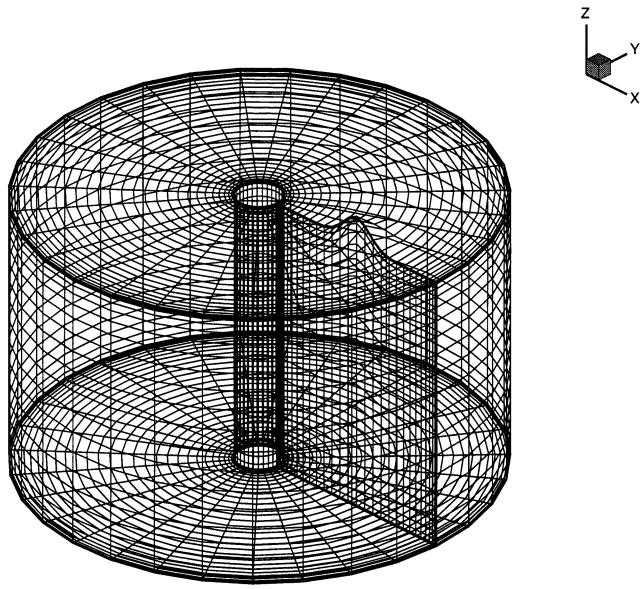

Figure 1. The three-dimensional pseudo-spectral σ-transformed mesh.

$$f^{n+1} = f^n + \frac{\Delta t}{12}\left[23\left.\frac{\mathrm{d}f}{\mathrm{d}t}\right|^n - 16\left.\frac{\mathrm{d}f}{\mathrm{d}t}\right|^{n-1} + 5\left.\frac{\mathrm{d}f}{\mathrm{d}t}\right|^{n-2}\right] + O(\Delta t^3) \tag{22}$$

in which n is the time index and Δt the time step. Using the AB3 method for updating the velocity potential at the free surface, we have $f^n = \Phi^n_{i,j,0}$, and the dynamic free surface boundary condition (14a) in discretized form gives

$$\begin{aligned}\left.\frac{\mathrm{d}f}{\mathrm{d}t}\right|^n = {} & \frac{\gamma^n_{i,j,0}}{h_{i,j}}\sum_{l=0}^{L}\hat{\boldsymbol{GZ}}^{(1)}_{0,l}\Phi^n_{i,j,l} + g\eta^n_{i,j} + \frac{2}{b}\left(\sum_{m=0}^{M}\hat{\boldsymbol{GR}}^{(1)}_{i,m}\Phi^n_{m,j,0} + \frac{\alpha_{i,j,0}}{h_{i,j}}\sum_{l=0}^{L}\hat{\boldsymbol{GZ}}^{(1)}_{0,l}\Phi^n_{i,j,l}\right)^2 \\ & + \frac{2}{q_i^2}\left(\sum_{n=0}^{N-1}\hat{\boldsymbol{G\theta}}^{(1)}_{j,n}\Phi^n_{i,n,0} + \frac{\beta_{i,j,0}}{h_{i,j}}\sum_{l=0}^{L}\hat{\boldsymbol{GZ}}^{(1)}_{0,l}\Phi^n_{i,j,l}\right)^2 + \frac{2}{h_{i,j}^2}\left(\sum_{l=0}^{L}\hat{\boldsymbol{GZ}}^{(1)}_{0,l}\Phi^n_{i,j,l}\right)^2\end{aligned} \tag{23}$$

Similarly, the updated free surface elevation is obtained as $f_n = \eta^n_{i,j}$ with the time derivative calculated from the discretized kinematic free surface condition (15) as

$$\begin{aligned}\left.\frac{\mathrm{d}f}{\mathrm{d}t}\right|^n = {} & \left(\frac{2}{h_{i,j}} - \frac{4\alpha_{i,j,0}}{b^2 h_{i,j}}\left.\frac{\partial\eta}{\partial R}\right|^n_{i,j} - \frac{4\beta_{i,j,0}}{q_i^2 h_{i,j}}\left.\frac{\partial\eta}{\partial\theta}\right|^n_{i,j}\right)\sum_{l=0}^{L}\hat{\boldsymbol{GZ}}^{(1)}_{0,l}\Phi^n_{i,j,l} - \frac{4}{b^2}\left.\frac{\partial\eta}{\partial R}\right|^n_{i,j}\sum_{m=0}^{M}\hat{\boldsymbol{GR}}^{(1)}_{i,m}\Phi^n_{m,j,0} \\ & - \frac{4}{q_i^2}\left.\frac{\partial\eta}{\partial\theta}\right|^n_{i,j}\sum_{n=0}^{N-1}\hat{\boldsymbol{G\theta}}^{(1)}_{j,n}\Phi^n_{i,n,0}\end{aligned} \tag{24}$$

After discretization using the pseudo-spectral matrix method, the transformed governing Equation (13a) becomes

$$\frac{1}{b^2}\sum_{m=0}^{M}\hat{\boldsymbol{GR}}^{(2)}_{i,m}\Phi_{m,j,k}+\frac{1}{q_i b}\sum_{m=0}^{M}\hat{\boldsymbol{GR}}^{(1)}_{i,m}\Phi_{m,j,k}+\frac{1}{q_i^2}\sum_{n=0}^{N-1}\hat{\boldsymbol{G\theta}}^{(2)}_{j,n}\Phi_{i,n,k}$$
$$+\left[\frac{1}{b^2 h_{i,j}}\left(\frac{\partial\alpha}{\partial R}\bigg|_{i,j,k}-2\frac{\alpha_{i,j,k}}{h_{i,j}}\frac{\partial\eta}{\partial R}\bigg|_{i,j}\right)+\frac{1}{q_i b}\frac{\alpha_{i,j,k}}{h_{i,j}}+\frac{1}{q_i^2 h_{i,j}}\left(\frac{\partial\beta}{\partial\theta}\bigg|_{i,j,k}-2\frac{\beta_{i,j,k}}{h_{i,j}}\frac{\partial\eta}{\partial\theta}\bigg|_{i,j}\right)\right]$$
$$\times\sum_{l=0}^{L}\hat{\boldsymbol{GZ}}^{(1)}_{k,l}\Phi_{i,j,l}+2\frac{\alpha_{i,j,k}}{b^2 h_{i,j}}\sum_{m=0}^{M}\sum_{l=0}^{L}\hat{\boldsymbol{GR}}^{(1)}_{i,m}\hat{\boldsymbol{GZ}}^{(1)}_{k,l}\Phi_{m,j,l}+2\frac{\beta_{i,j,k}}{q_i^2 h_{i,j}}\sum_{n=0}^{N-1}\sum_{l=0}^{L}\hat{\boldsymbol{G\theta}}^{(1)}_{j,n}\hat{\boldsymbol{GZ}}^{(1)}_{k,l}\Phi_{i,n,l}$$
$$+\left[\left(\frac{\alpha_{i,j,k}}{b h_{i,j}}\right)^2+\left(\frac{\beta_{i,j,k}}{q_i h_{i,j}}\right)^2+\frac{1}{h_{i,j}^2}\right]\sum_{l=0}^{L}\hat{\boldsymbol{GZ}}^{(2)}_{k,l}\Phi_{i,j,l}=0 \tag{25}$$

where $\hat{\boldsymbol{GR}}$ and $\hat{\boldsymbol{GZ}}$ are Chebyshev pseudo-spectral matrices and $\hat{\boldsymbol{G\theta}}$ is a Fourier pseudospectral matrix. Note that

$$\frac{\partial\alpha}{\partial R}\bigg|_{i,j,k}=-(\sigma_k+1)\sum_{m=0}^{M}\hat{\boldsymbol{GR}}^{(2)}_{i,m}\eta_{m,j},\qquad \frac{\partial\beta}{\partial\theta}\bigg|_{i,j,k}=-(\sigma_k+1)\sum_{n=0}^{N-1}\hat{\boldsymbol{G\theta}}^{(2)}_{j,n}\eta_{i,n} \tag{26}$$

$$\frac{\partial\eta}{\partial R}\bigg|_{i,j}=\sum_{m=0}^{M}\hat{\boldsymbol{GR}}^{(1)}_{i,m}\eta_{m,j}\quad\text{and}\quad\frac{\partial\eta}{\partial\theta}\bigg|_{i,j}=\sum_{n=0}^{N-1}\hat{\boldsymbol{G\theta}}^{(1)}_{j,n}\eta_{i,n} \tag{27}$$

The bottom boundary condition is discretized as

$$\sum_{l=0}^{L}\hat{\boldsymbol{GZ}}^{(1)}_{L,l}\Phi_{i,j,l}=0 \tag{28}$$

The discretized solid wall boundary conditions are

$$\sum_{m=0}^{M}\hat{\boldsymbol{GR}}^{(1)}_{i,m}\Phi_{m,j,k}+\frac{\alpha_{i,j,k}}{h_{i,j}}\sum_{l=0}^{L}\hat{\boldsymbol{GZ}}^{(1)}_{k,l}\Phi_{i,j,l}=0 \tag{29}$$

where $i=M$ refers to the inner cylinder at $R=-1$ and $i=0$ refers to the outer cylindrical perimeter at $R=1$. For the open domain problem, the σ-transformed Sommerfeld boundary condition (18) is discretized to give updated far boundary nodal values using the AB3 method from $f^n=\Phi^n_{0,j,k}$, where

$$\frac{\mathrm{d}f}{\mathrm{d}t}\bigg|^n=-\frac{\gamma^n_{0,j,k}}{h_{0,j}}\sum_{l=0}^{L}\hat{\boldsymbol{GZ}}^{(1)}_{k,l}\Phi^n_{0,j,l}-c\left(\sum_{m=0}^{M}\hat{\boldsymbol{GR}}^{(1)}_{0,m}\Phi^n_{m,j,k}+\frac{\alpha_{0,j,k}}{h_{0,j}}\sum_{l=0}^{L}\hat{\boldsymbol{GZ}}^{(1)}_{k,l}\Phi^n_{0,j,l}\right) \tag{30}$$

The pressure distribution at the $n+1$th time step is discretized as

$$p_{j,k}^{n+1} = -\rho g\left[\frac{h_{M,j}^{n+1}(\sigma_k^{n+1}+1)}{2} - d\right]$$

$$-\frac{\rho}{2}\left[\frac{2}{q_M}\left(\sum_{n=0}^{N-1}\hat{\boldsymbol{G}}\boldsymbol{\theta}_{j,n}^{(1)}\Phi_{M,n,k}^{n+1} + \frac{\beta_{M,j,k}}{h_{M,j}}\sum_{l=0}^{L}\hat{\boldsymbol{G}}\boldsymbol{Z}_{k,l}^{(1)}\Phi_{M,j,l}^{n+1}\right)^2 + \left(\frac{2}{h_{M,j}^{n+1}}\sum_{l=0}^{L}\hat{\boldsymbol{G}}\boldsymbol{Z}_{k,l}^{(1)}\Phi_{M,j,l}^{n+1}\right)^2\right]$$

$$-\frac{\rho(\Phi_{M,j,k}^{n+1} - \Phi_{M,j,k}^{n})}{\Delta t} - \frac{\rho\gamma_{M,j,k}^{n+1}}{h_{M,j}^{n+1}}\sum_{l=0}^{L}\hat{\boldsymbol{G}}\boldsymbol{Z}_{k,l}^{(1)}\Phi_{M,j,l}^{n+1} \tag{31}$$

The horizontal force components are evaluated using double quadrature formulae: Simpson's rule is applied in the angular direction, and the trapezoidal rule used in vertical direction.

Starting from a prescribed initial wave form, the solution procedure is as follows: (i) calculate free surface boundary values of Φ using Equation (23); (ii) update the surface elevation, η, using Equation (24); (iii) solve the discrete governing Equation (25) together with the bed and wall boundary conditions (28) and (29) by an iterative matrix solver; (iv) evaluate the total force acting on the bottom-mounted cylinder; and (v) move forward one time step and return to (i). In producing the results discussed below, successive over-relaxation (SOR) was used as the iterative matrix solver.

4. RESULTS

In all cases, the results are presented in non-dimensional form. Taking the characteristic length to be d, and the characteristic time to be $(d/g)^{1/2}$, then the non-dimensionalized potential function is $d(gd)^{1/2}\Phi$ and the non-dimensional free surface elevation is η/d where d is the still water depth. Two initial wave profiles were used to illustrate use of the model. The first is an axisymmetric sloshing case for which an analytical potential theory solution to second-order has been derived by Ma and Wu [6]. The second starts from an asymmetric impulse-like free surface disturbance and involves complex interactions between wave reflection and diffraction effects.

4.1. Axisymmetric standing waves in a cylindrical tank with a surface-piercing column at its centre

In order to test the numerical model, an initial wave profile is imposed on the free surface which may be expressed as

$$\eta(r, \theta, t=0) = aZ_k(r) \tag{32}$$

where a is the amplitude of the initial wave and

$$Z_k(r) = J_0(\alpha_k r) + B_k Y_0(\alpha_k r) \tag{33}$$

J_0, J_1, Y_0 and Y_1 are Bessel functions of the first and second kind respectively. B_k and α_k are obtained from the boundary conditions on the walls of the inner and outer cylinders, of radii r_I and r_O respectively. This leads to:

$$B_k = -\frac{J_1(\alpha_k r_I)}{Y_1(\alpha_k r_I)} \tag{34}$$

where α_k are solutions of

$$J_1(\alpha_k r_O) + B_k Y_1(\alpha_k r_O) = 0 \tag{35}$$

This axisymmetric problem has been solved analytically using a perturbation technique [6]. The linear solution is obtained by means of the variable separation method. The first-order solution is

$$\eta_1 = aZ_k(r)\cos(\omega_k t) \tag{36}$$

where

$$\omega_k^2 = g\alpha_k \tanh(\alpha_k d) \tag{37}$$

The second-order elevation, η_2, is

$$\eta_2 = \eta_2^{(1)} + \eta_2^{(2)} \tag{38}$$

where

$$\eta_2^{(1)} = -\frac{1}{g}\left[\eta_1 \frac{\partial^2 \phi_1}{\partial z\, \partial t} + \frac{1}{2}|\nabla \phi_1|^2\right]_{z=0} \quad \text{and} \quad \eta_2^{(2)} = -\frac{1}{g}\frac{\partial \phi}{\partial t}\bigg|_{z=0} \tag{39}$$

In Equation (39), ϕ_1 and ϕ_2 are the first- and second-order solutions for the velocity potential. Ma and Wu [6] gave details of the second-order solution.

The non-dimensional radii of the inner cylinder r_I/d and of the cylindrical tank r_O/d are 0.4 and 2 respectively for the cases studied below. The convergence criterion in the iterative matrix solver is set at 10^{-9}. From convergence tests using time-evolving plots of surface deformation at a specific point in the tank (the surface of the inner cylinder), grid and time step independence was achieved for non-dimensional time step 0.02 and a grid ($M \times N \times L$) of ($21 \times 11 \times 11$) collocation points. These values are used hereafter.

Three cases with different amplitudes a/d, 0.01, 0.15 and 0.2, are considered in order to examine increasingly non-linear effects. The time history of the runup on the surface of the inner cylinder is calculated both numerically and from the linear analytical solution. The results are independent of their circumferential position on the inner cylinder as the problem is axisymmetric. The time history of runup at the inner cylinder shown in Figure 2 reveals almost exact agreement between the numerical and analytical linear theory results for the

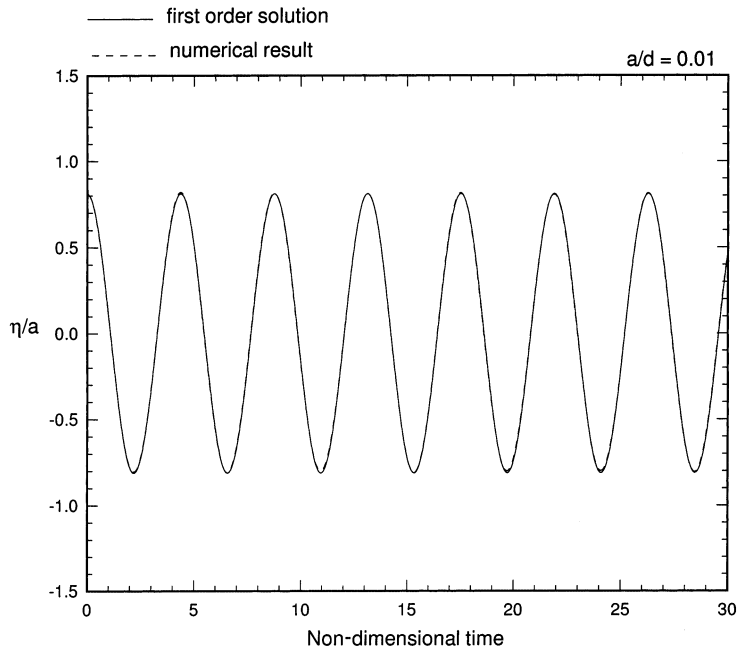

Figure 2. Time-dependent run-up for the axisymmetric case: $a/d = 0.01$.

smallest amplitude case where $a/d = 0.01$. Figure 3 shows the numerically derived free surface profiles radially across the tank (at $\theta = 0$) at different times during a wave period, for the same initial wave. A node is found at $r/d = 1.32$. Figure 4 reveals non-linearities in the run-up time history at the inner cylinder surface for the case $a/d = 0.15$; the linear and second-order non-linear solutions are seen to have different profiles after $t^* = t(d/g)^{1/2} = 1$. The numerical solution is very close to the second-order non-linear solution except at some wave peaks. Figure 5 shows the wave profiles radially across the tank at $\theta = 0$, again at different times during the wave period. The node at $r/d = 1.32$ disappears due to the non-linearity of the waves. Returning to Figure 4, it is clear that the second-order analytical solution is not sufficient to describe large amplitude free surface motions completely. A fully non-linear wave model is necessary in such cases. Figure 6 shows the time histories of runup at the inner cylinder for three amplitude ratios, $a/d = 0.01$, 0.15 and 0.2. In general, as the wave amplitude increases, the peaks become higher and the troughs shallower. Moreover, higher-order effects become increasingly evident at large wave amplitude, as can be seen by the variations in successive wave profile. This is similar to the two-dimensional standing wave cases considered by Chern *et al.* [21].

It may be concluded that the above cases partially validate the three-dimensional numerical scheme in the case of axisymmetry. It should be noticed that the proposed numerical model is able to deal with non-linear free surface waves without requiring the surface smoothing mentioned by Longuet-Higgins and Cokelet [26].

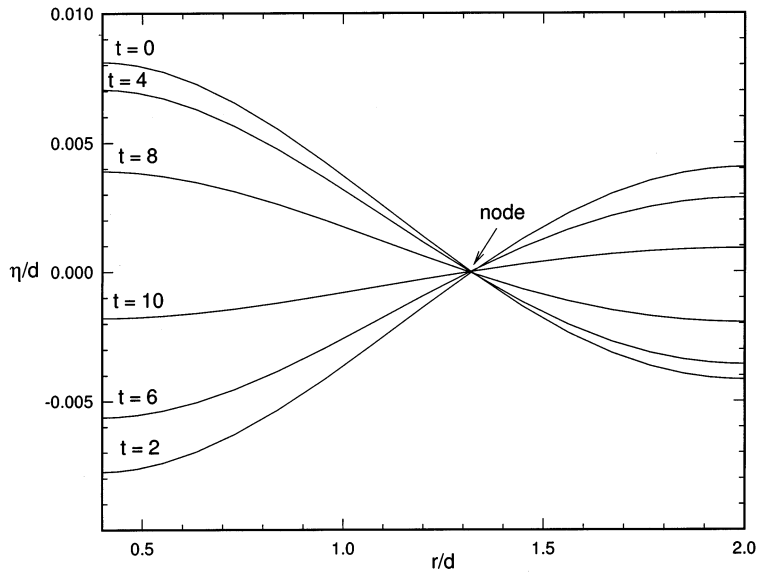

Figure 3. Wave profile evolution for the axisymmetric case: $a/d = 0.01$.

4.2. Asymmetric initial impulse wave in a cylindrical tank with a surface-piercing cylinder at its centre

Figure 7 shows the asymmetric impulse wave free surface which is used as the initial condition here. This case has been studied by Yu and Yeung [17], and causes diffraction around the inner cylinder. The formula for the initial wave form is taken to be the following:

$$\eta(r, \theta, t = 0) = a \exp\left[-\left[r \cos\theta - \frac{(r_I + r_O)}{2} \right]^2 - [r \sin\theta]^2 \right] \tag{40}$$

The radii of the inner and outer walls are $r_I/d = 1$ and $r_O/d = 10$ respectively. The peak of the impulse wave is located at the middle of the radial line between the inner cylinder and the cylindrical tank perimeter wall ($r = 5.5$, $\theta = 0$). The non-dimensional time step is 0.01. The amplitude of the initial wave, a/d, is 0.1. A grid containing $41 \times 31 \times 17$ collocation points comprises the computational domain. Figures 8(a)–(j) present the evolution of the free surface wave pattern at intervals of 300 time steps (a non-dimensional interval of 3). An outgoing ring wave develops by $t^* = t(g/d)^{1/2} = 3$ as illustrated in Figure 8(a). The outgoing wave interacts with the cylinder in Figure 8(b) and also begins to reflect from the perimeter wall of the cylindrical tank. Diffraction due to the ring wave is observed in Figures 8(c)–(e) from $t^* = 9$ to 15. In addition, the reflected waves from the cylindrical tank wall appear to become parallel and straight relative to each other after $t^* = 15$ in Figures 8(f)–(i). This may be explained by analogy with optical theory, where the impulse wave can be regarded as a point light source

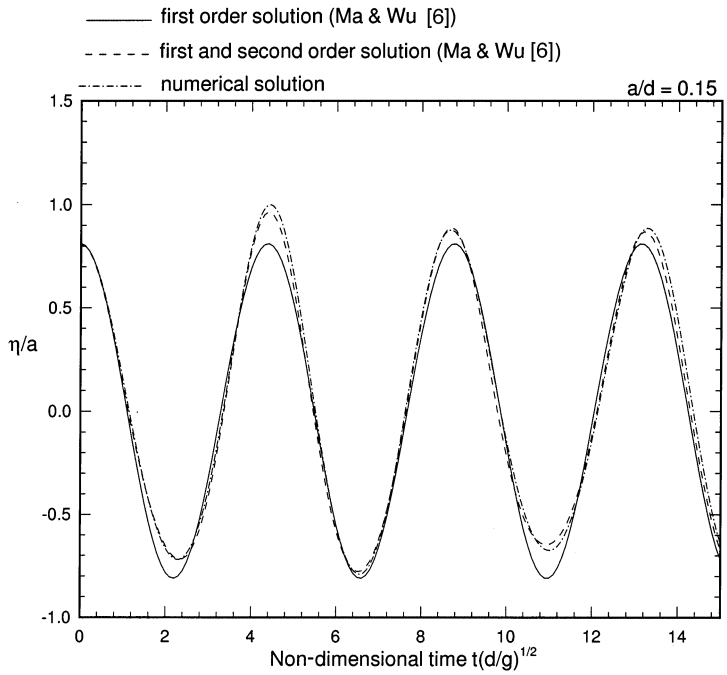

Figure 4. Time-dependent run-up for the axisymmetric case: $a/d = 0.15$.

and the reflection waves are plane waves caused when the point source is located in front of a semi-circular mirror. Later (from $t^* = 2$), the plane waves reflecting from the outer cylindrical tank hit the inner cylinder and cause further diffraction (see Figures 8(g)–(j)). Yu and Yeung [17] also observed the same phenomenon. In order to aid quantification of the numerical results, Figures 9(a) and (b) are contour plots of free surface elevation at $t^* = 15$ and 30 respectively; these provide a clear picture of the evolving free surface patterns. Taken overall, the free surface exhibits complicated wave phenomena as time progresses due to the initial disturbance.

The time history of horizontal force acting on the inner cylinder is presented in Figure 10. The first peak is caused by the outgoing ring wave. Later peaks, which are higher, are caused by the combination of incident, reflected and diffracted waves.

4.3. Asymmetric initial impulse wave in an infinite domain with a surface-piercing cylinder at its centre

The previous two cases deal with wave motions confined within a cylindrical tank. The third case considers free surface motions in an infinite domain. The previous impulse wave is still used as the initial wave condition. The infinite physical domain is modelled as a finite, but open, computational domain. The peak of the impulse wave is now taken (at $r/d = 5.0$, $\theta = 0$), so that in other words,

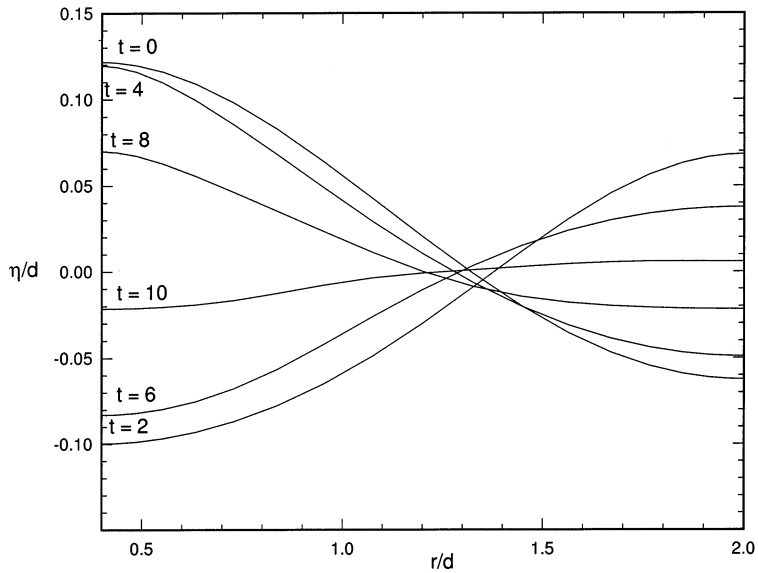

Figure 5. Wave profile evolution for the axisymmetric case: $a/d = 0.15$.

$$\eta(r, \theta, t = 0) = a \exp[-[r \cos \theta - 5]^2 - [r \sin \theta]^2] \tag{41}$$

The outer radius is 20 times the inner radius ($r_I/d = 1$). The Sommerfeld radiation condition is imposed at the open boundary to avoid the reflection of outgoing waves, with the phase velocity $c = (gh)^{1/2}$ corresponding to shallow water condition. In addition, 0.01 is chosen as the dimensionless time step and the mesh is again taken as $41 \times 31 \times 17$.

Figures 11(a)–(j) show shaded plots of the evolution from $t^* = 3$ to 30. Similar to the case in the cylindrical tank, a ring outgoing wave initially forms as indicated in Figure 11(a). Subsequently, the ring wave expands and interacts with the surface-piercing cylinder. Diffraction around the cylinder is observed in the simulation. Selected contour plots at $t^* = 15$ and 30 are presented in Figures 12(a) and (b) respectively. No reflected waves are evident at the far-field boundary, thus confirming the successful implementation of the radiation condition.

The force time history is presented in Figure 13. The initial peak force in the trace is almost identical to that obtained for the closed tank. However, the effect of the open boundary can be seen at later times when the free surface rapidly settles down, unlike the situation in the closed tank where oscillations are still very large at $t^* = 30$. It should be noted that the Sommerfeld radiation condition used herein is suitable only for shallow water waves, but with an appropriate choice of phase velocity other conditions could be modelled.

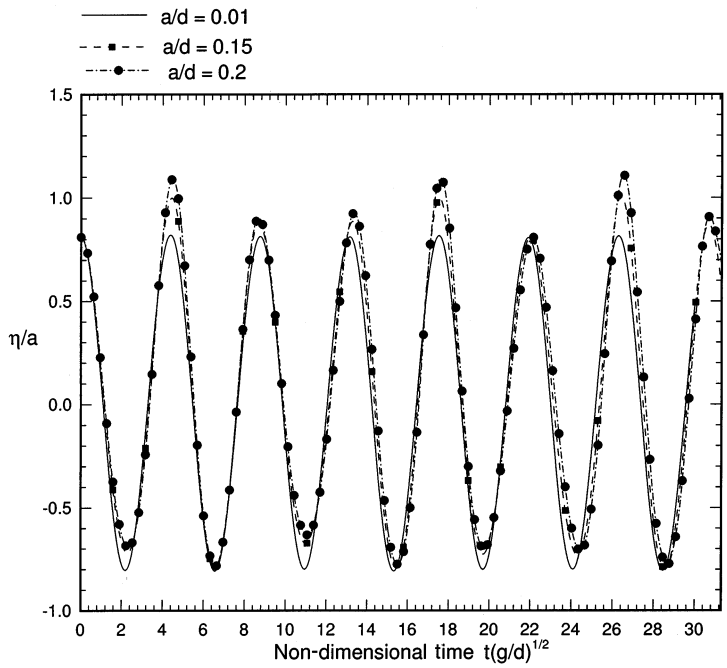

Figure 6. Time-dependent run-up for the axisymmetric case: $a/d = 0.01$, 0.15 and 0.2.

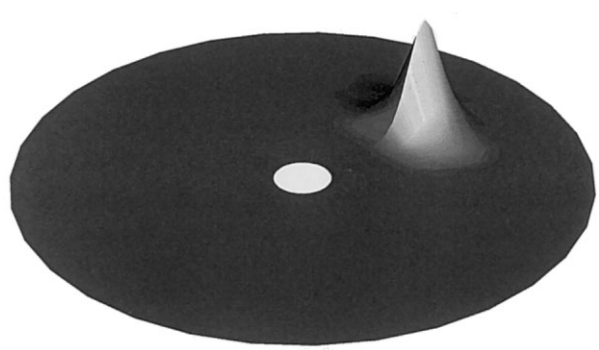

Figure 7. A shaded plot of the initial asymmetric impulse wave profile. The free surface profile is exaggerated (by scaling the vertical dimension by 40).

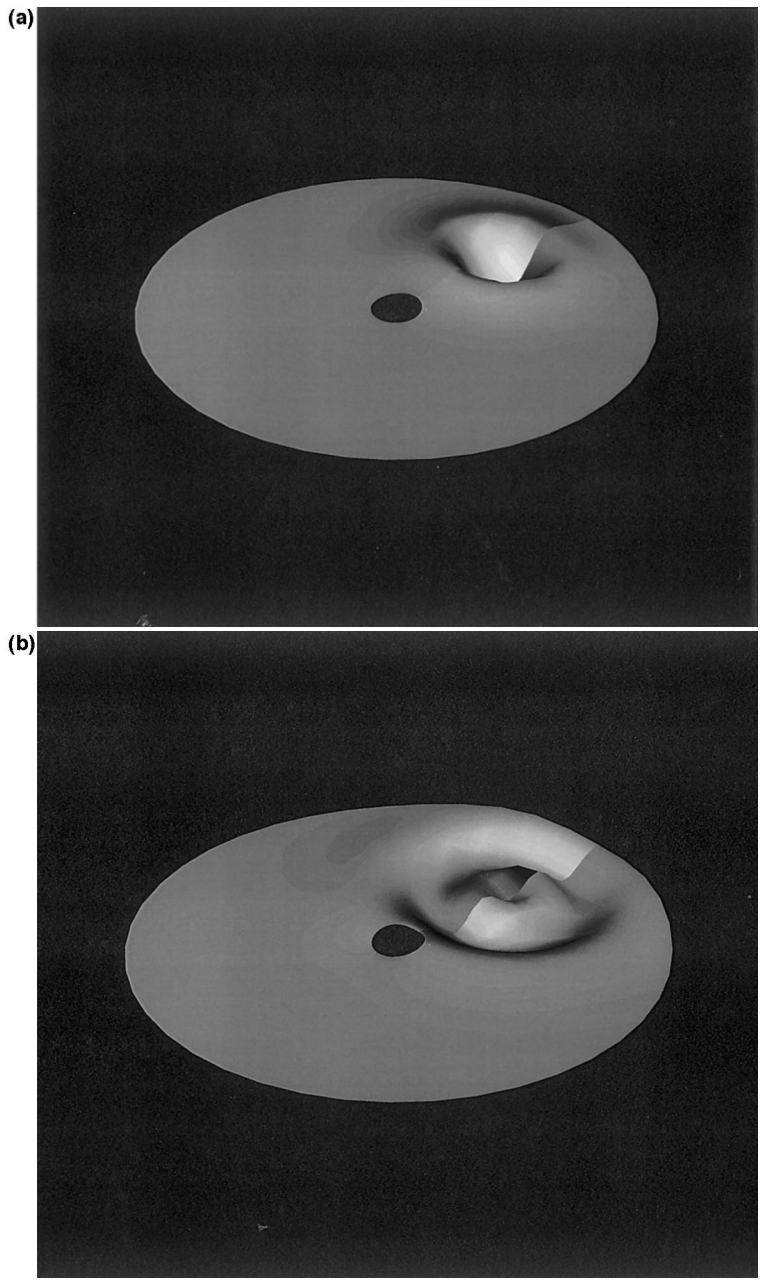

Figure 8. Three-dimensional shaded plots of the asymmetric impulse wave evolution in a closed cylindrical tank containing a surface-piercing cylinder at its centre: (a) $t^* = t(g/d)^{1/2} = 3$; (b) $t^* = t(g/d)^{1/2} = 6$; (c) $t^* = t(g/d)^{1/2} = 9$; (d) $t^* = t(g/d)^{1/2} = 12$; (e) $t^* = t(g/d)^{1/2} = 15$; (f) $t^* = t(g/d)^{1/2} = 18$; (g) $t^* = t(g/d)^{1/2} = 21$; (h) $t^* = t(g/d)^{1/2} = 24$; (i) $t^* = t(g/d)^{1/2} = 27$; (j) $t^* = t(g/d)^{1/2} = 30$.

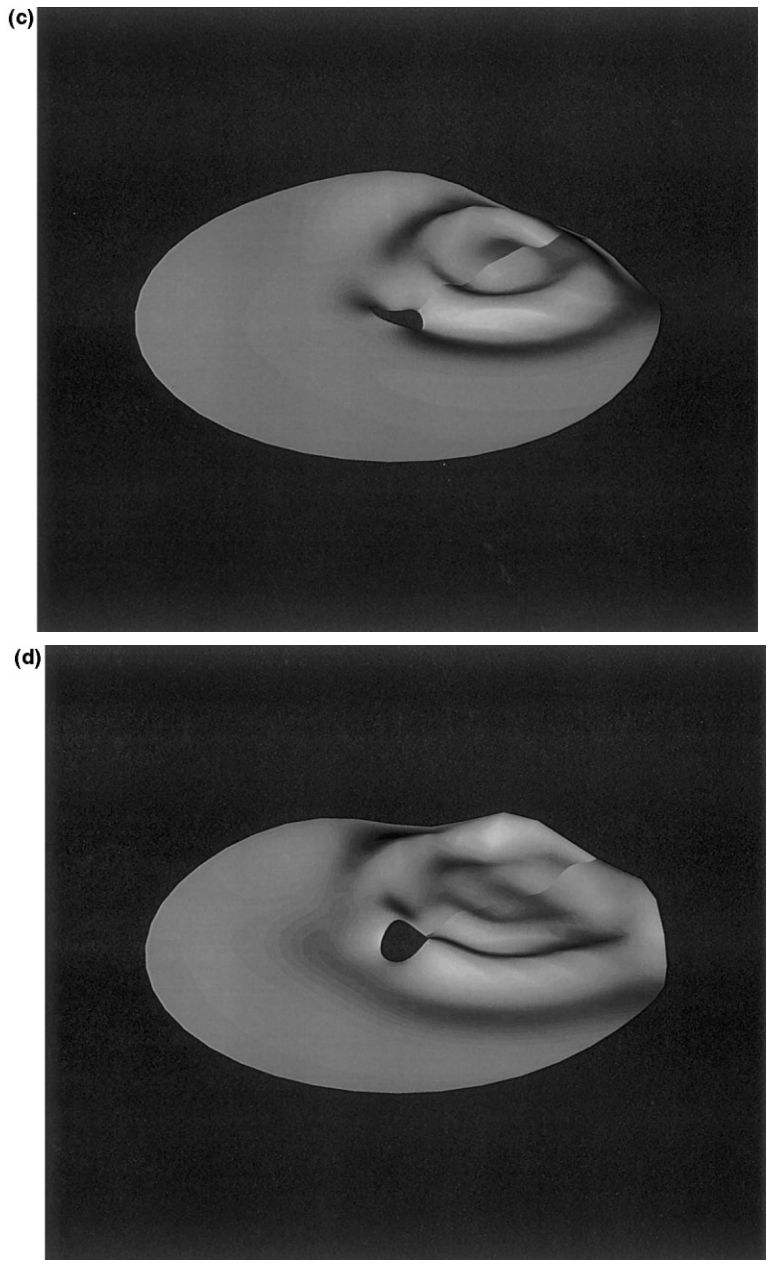

Figure 8 (*Continued*)

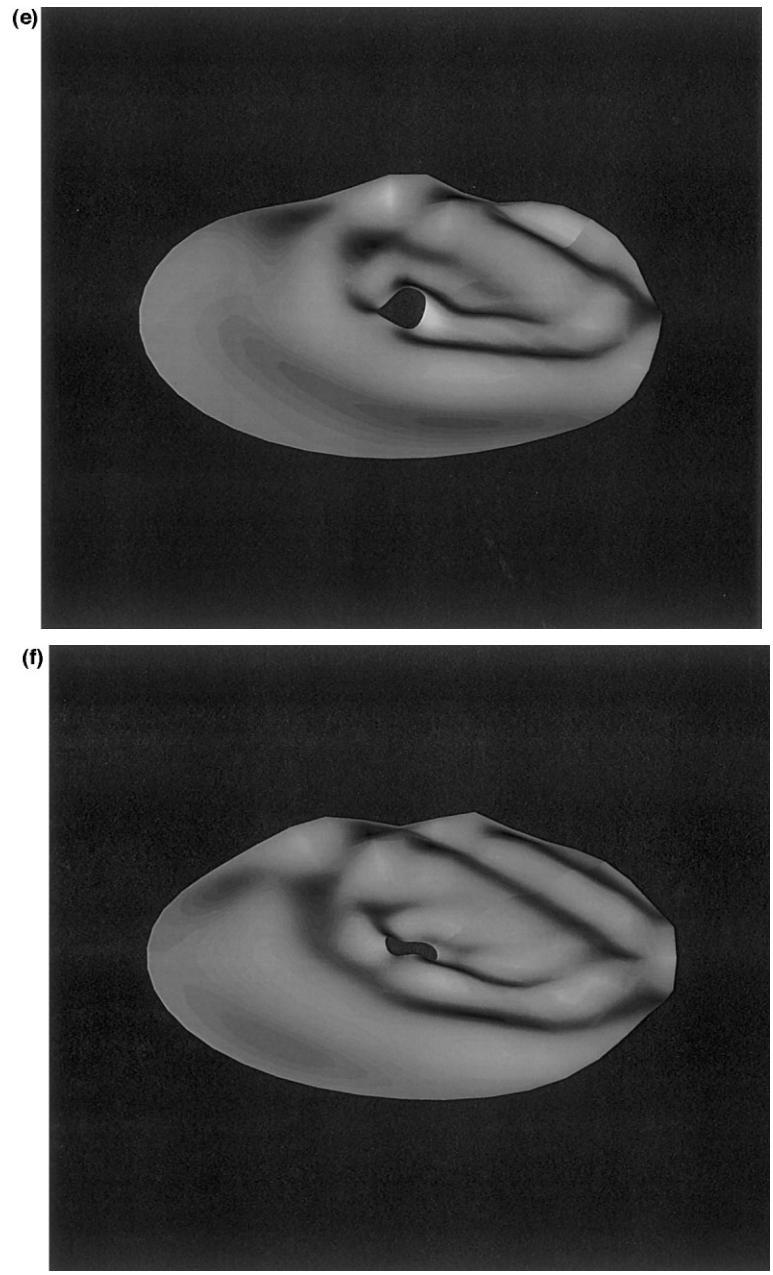

Figure 8 (*Continued*)

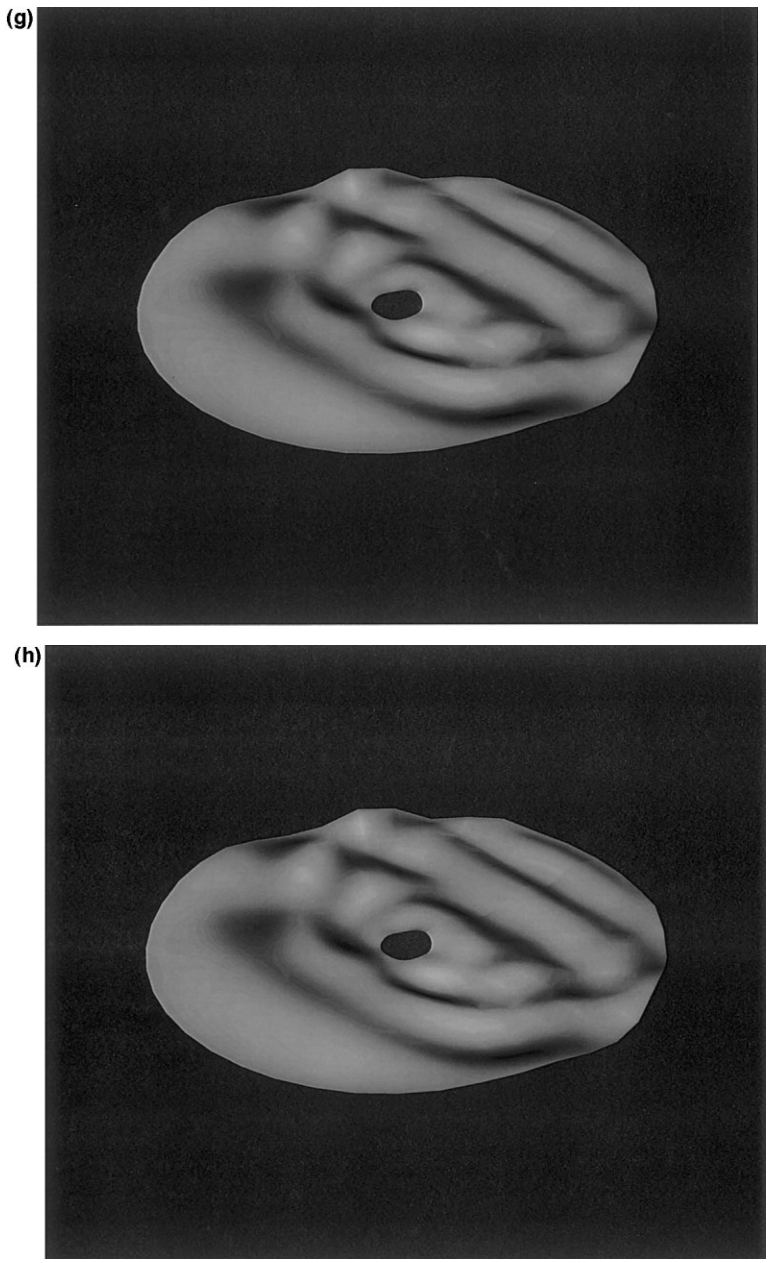

Figure 8 (*Continued*)

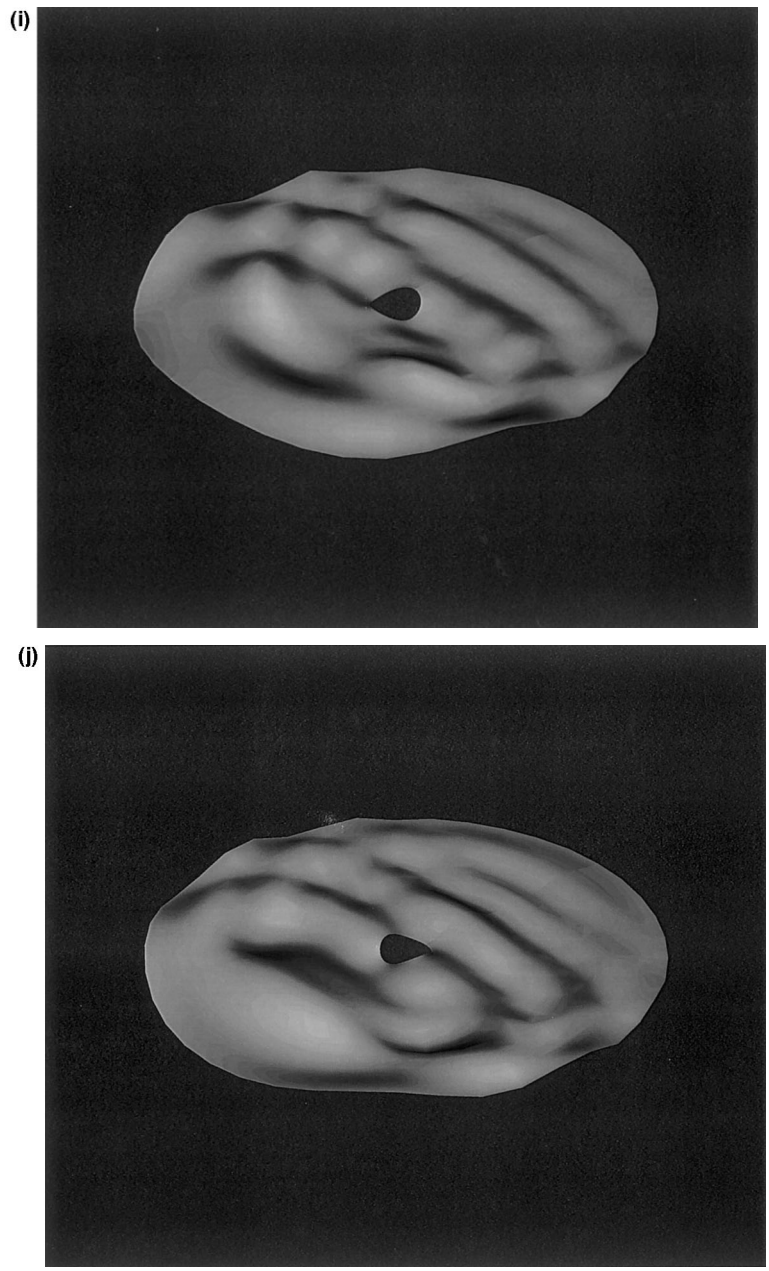

Figure 8 (*Continued*)

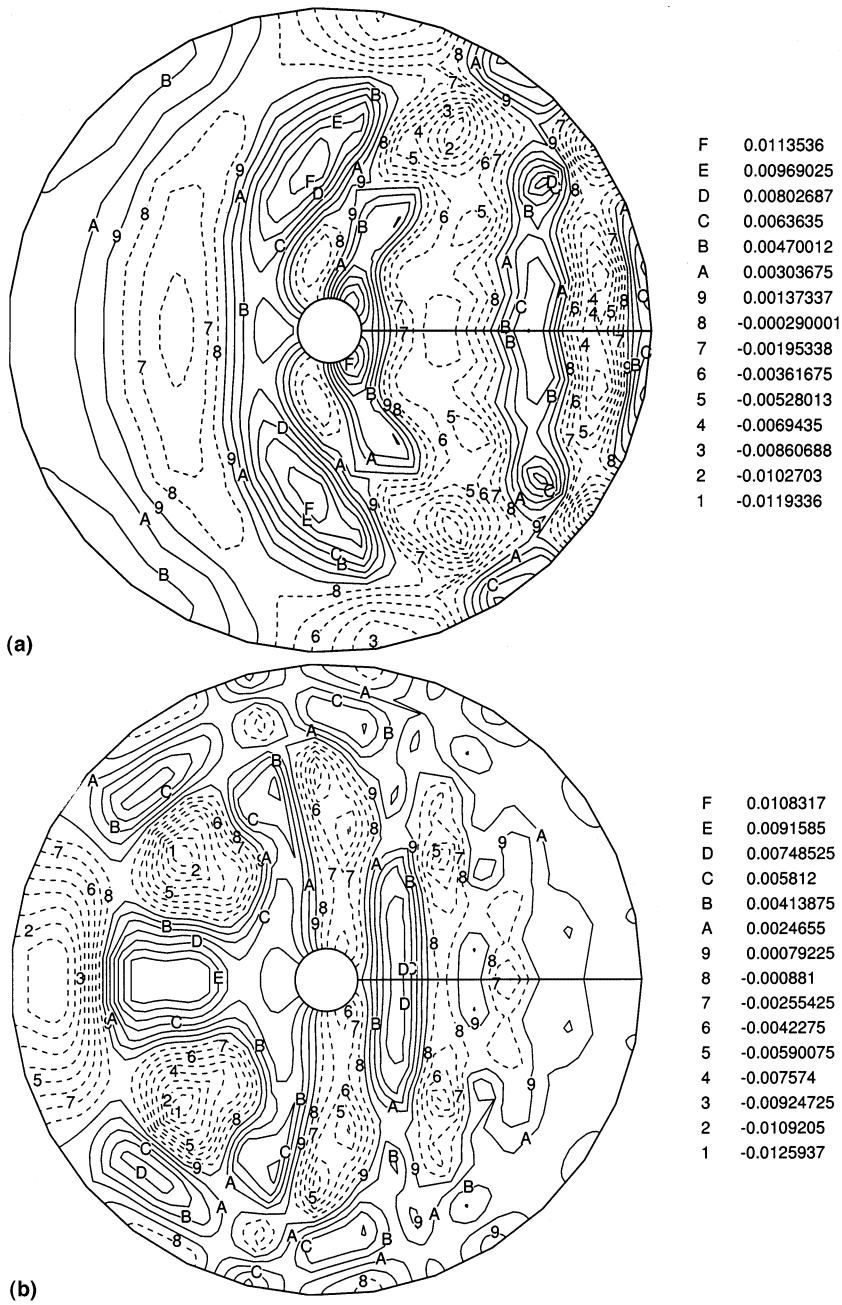

Figure 9. Free surface contours for an asymmetric impulse wave in the closed tank. Solid lines represent positive surface elevation values, dashed lines negative: (a) $t^* = t(g/d)^{1/2} = 15$; (b) $t^* = t(g/d)^{1/2} = 30$.

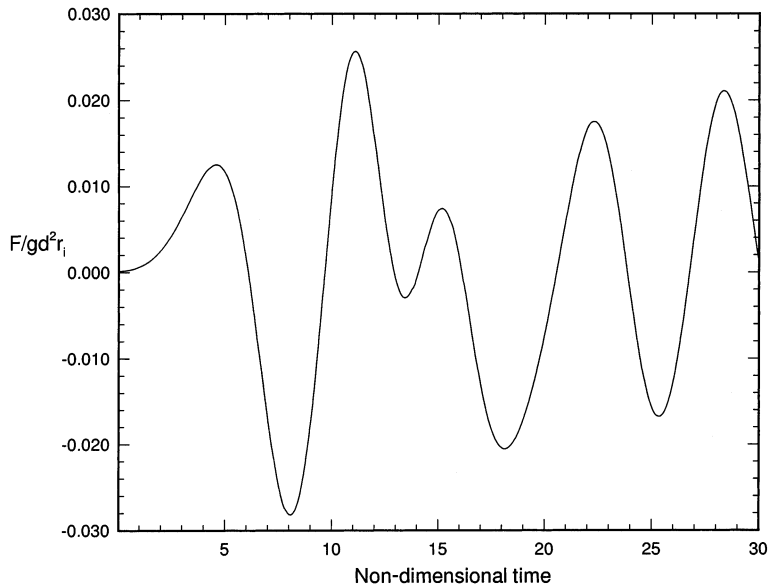

Figure 10. Time history of the x-direction force component acting on inner cylinder for the asymmetric case in the cylindrical tank.

5. CONCLUSIONS

A σ-transformed mathematical model is proposed here for three-dimensional non-overturning free surface waves in a cylindrical domain containing a central surface-piercing circular cylinder, and with solid wall or open perimeter boundaries. The model has been discretized using the collocation (or pseudo-spectral) matrix element method with Chebyshev matrices in the radial and vertical directions and Fourier matrices in the angular direction. Before application to wave problems the pseudo-spectral scheme has been tested successfully against standard solutions of Laplace's equation on square and annular two-dimensional domains. The numerical model was then used to simulate sloshing waves in a cylindrical tank containing a surface-piercing central column. The results were in extremely close agreement with Ma and Wu's [6] second-order potential theory solution for waves of small amplitude ($a/d < 0.01$). At higher wave amplitudes, the numerical scheme predicted an increasing contribution from higher-order (i.e. greater than 2) non-linear effects, with wave crests narrowing and steepening, and wave troughs becoming shallower than predicted by second-order potential theory. The numerical scheme was then applied to the case of an initial asymmetric impulse wave in an annular tank. Unsurprisingly, the free surface motions grow in complexity with time; a ring wave forms which is reflected by the solid walls and diffracted by the central cylinder. At one

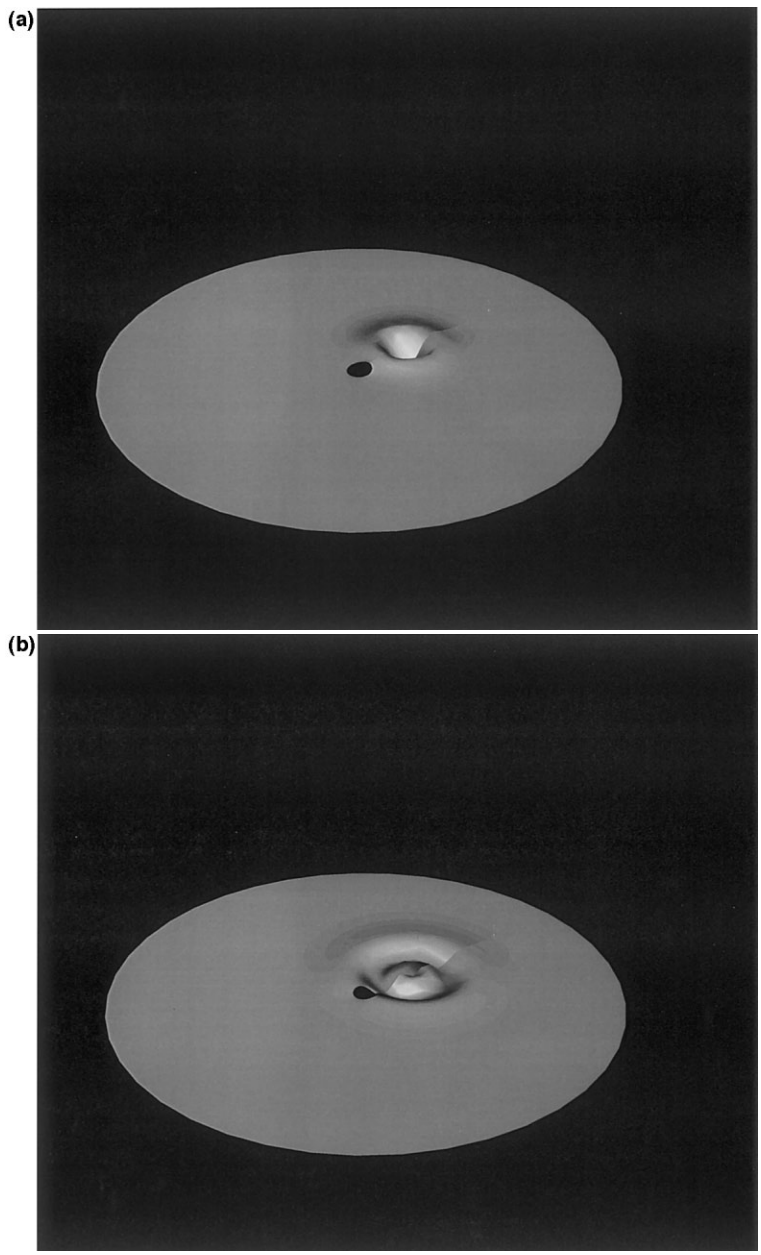

Figure 11. Three-dimensional shaded plots of the asymmetric impulse wave evolution in an open cylindrical domain containing a surface-piercing cylinder at its centre: (a) $t^* = t(g/d)^{1/2} = 3$; (b) $t^* = t(g/d)^{1/2} = 6$; (c) $t^* = t(g/d)^{1/2} = 9$; (d) $t^* = t(g/d)^{1/2} = 12$; (e) $t^* = t(g/d)^{1/2} = 15$; (f) $t^* = t(g/d)^{1/2} = 18$; (g) $t^* = t(g/d)^{1/2} = 21$; (h) $t^* = t(g/d)^{1/2} = 24$; (i) $t^* = t(g/d)^{1/2} = 27$; (j) $t^* = t(g/d)^{1/2} = 30$.

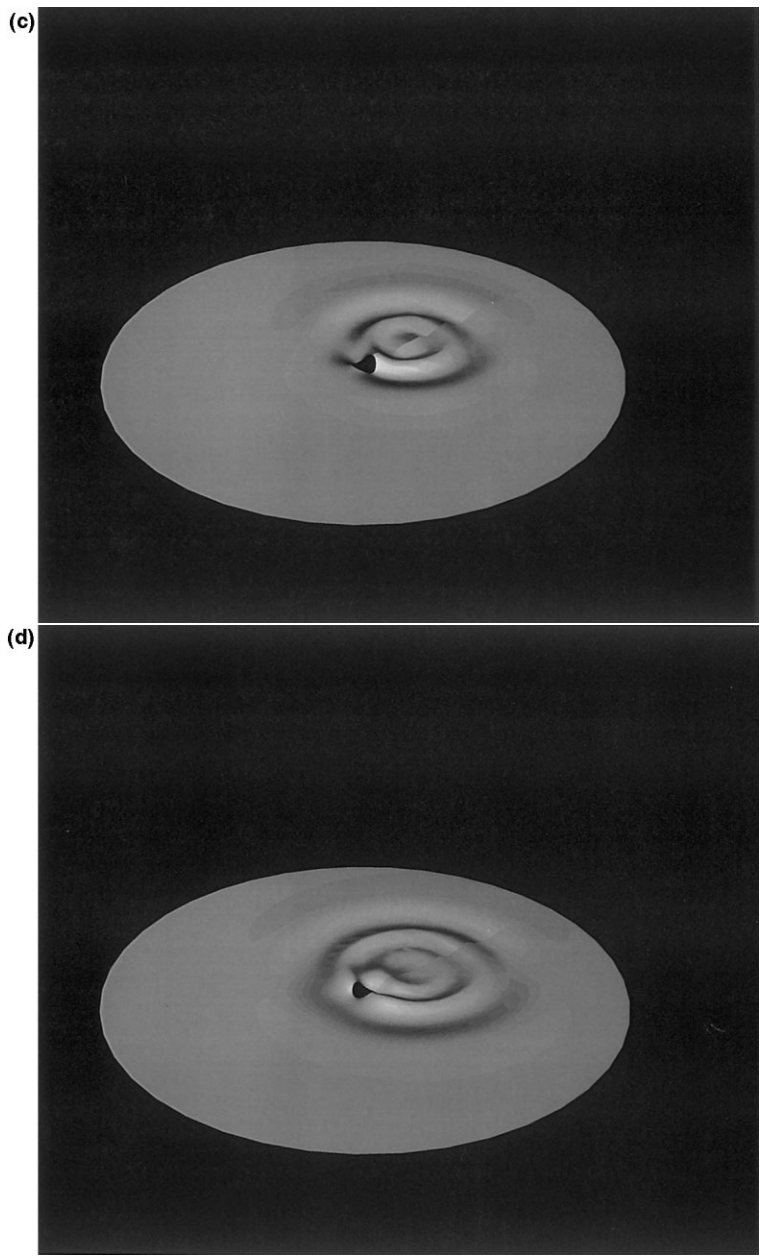

Figure 11 (*Continued*)

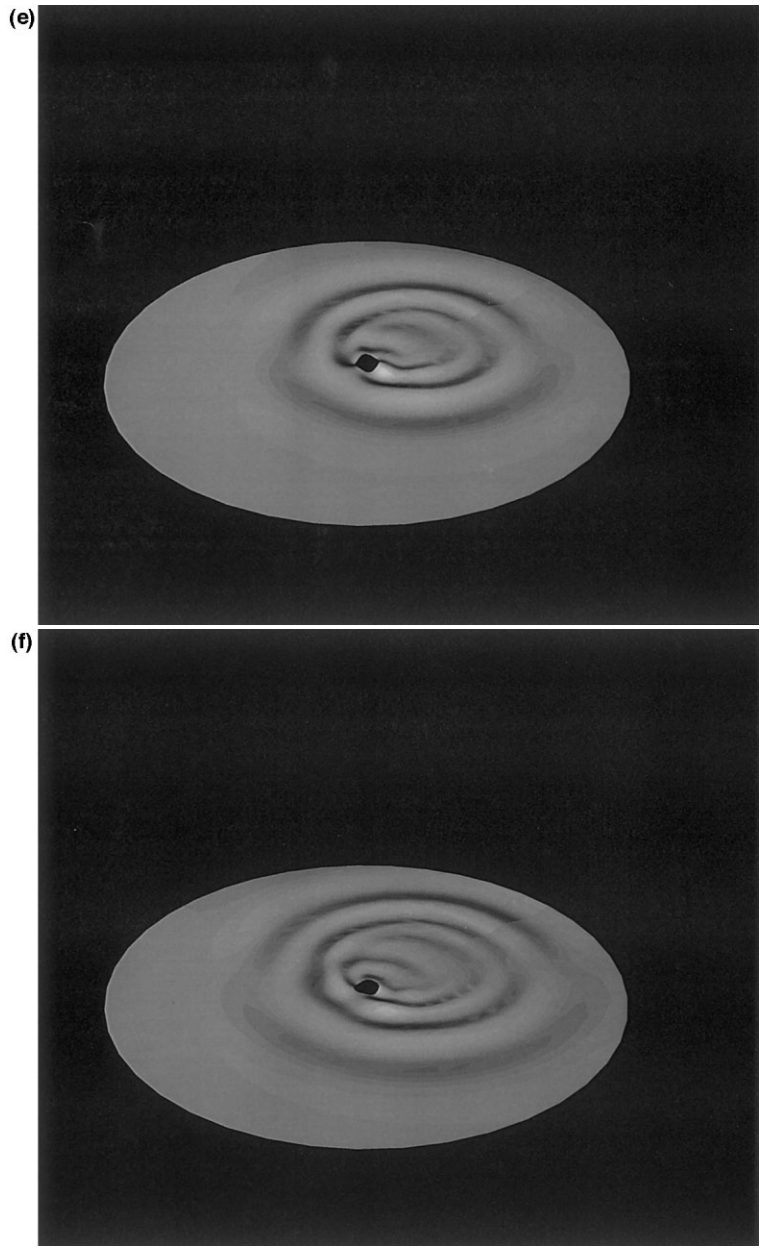

Figure 11 (*Continued*)

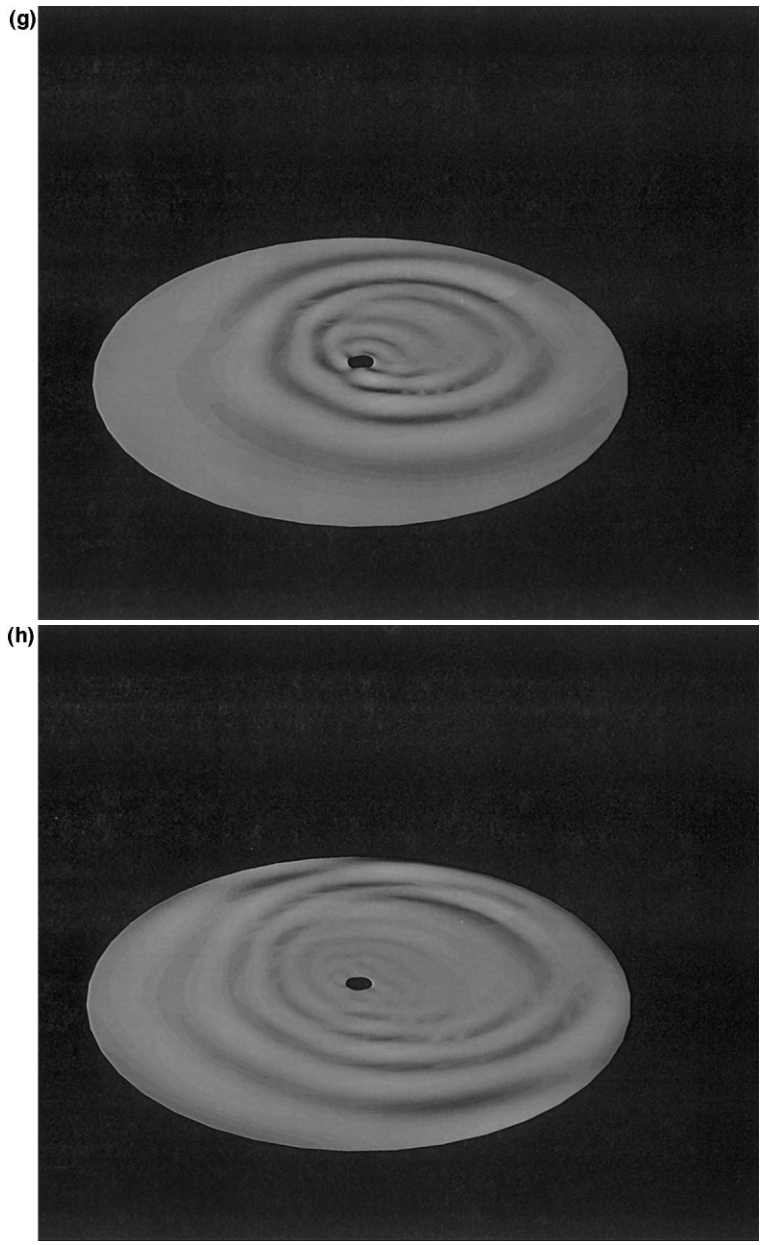

Figure 11 (*Continued*)

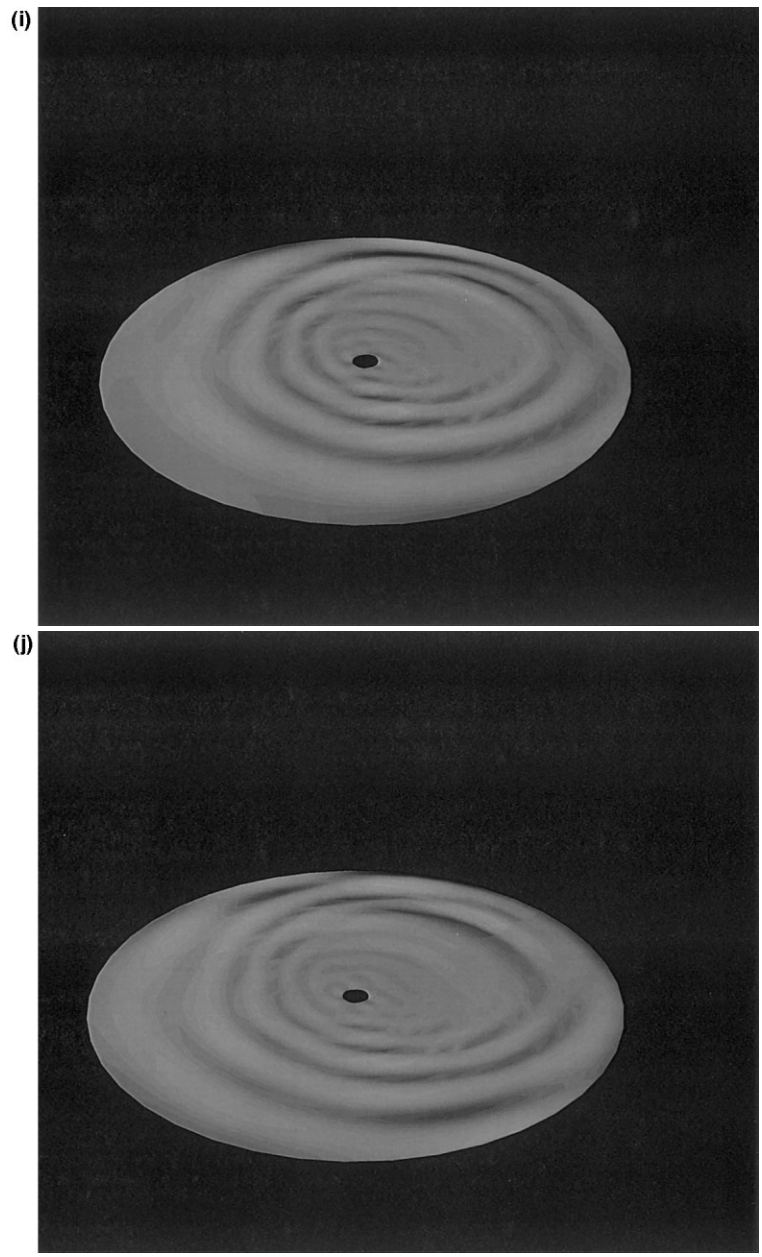

Figure 11 (*Continued*)

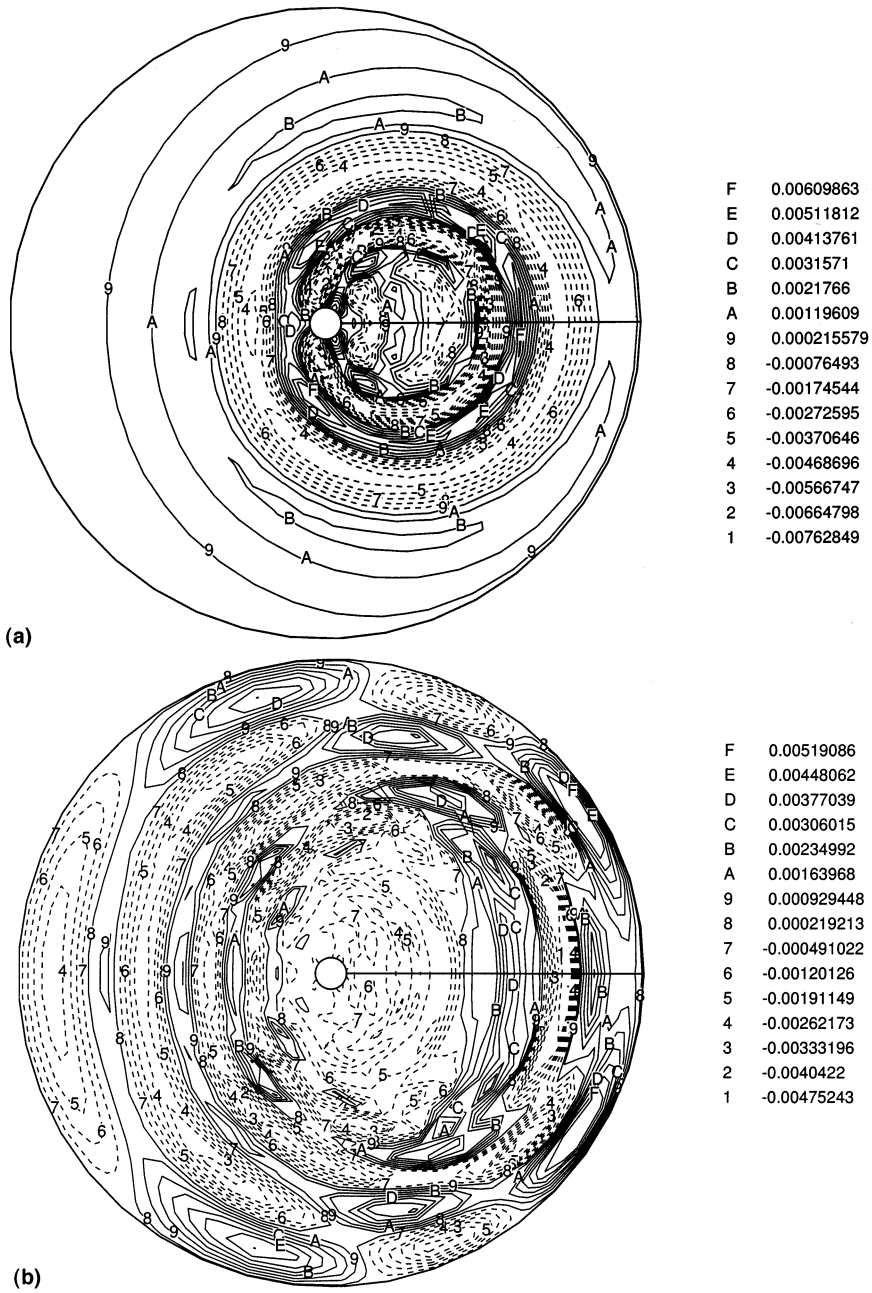

Figure 12. Free surface contours for an asymmetric impulse wave in the open domain. Solid lines represent positive surface elevation values, dashed lines negative: (a) $t^* = t(g/d)^{1/2} = 15$; (b) $t^* = t(g/d)^{1/2} = 30$.

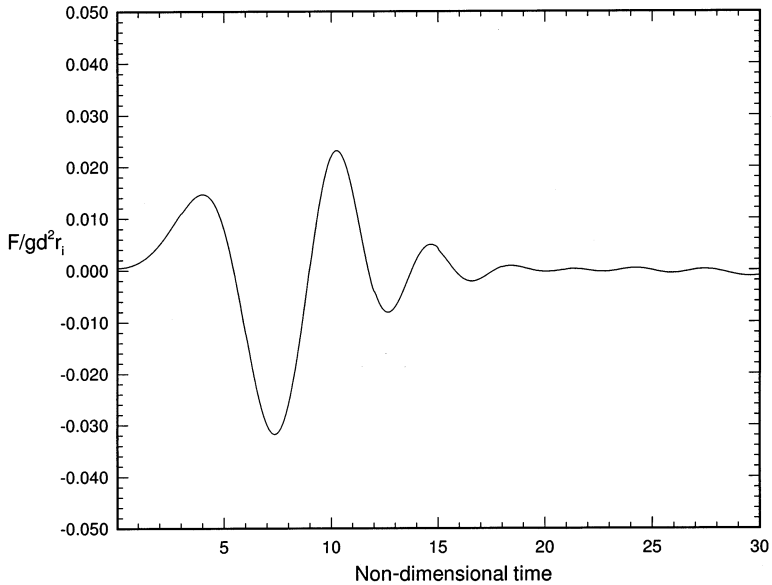

Figure 13. Time history of x-direction force component acting on the cylinder for the asymmetric case in the open domain.

stage in the process, plane waves appear behind the central cylinder. In the final case, the outer wall perimeter is replaced by an open boundary, and the test repeated. Whereas the initial stages of the free surface development are similar to the closed tank case, the open boundary permits waves to exit the domain and it is seen that the free surface disturbances settle quickly. In the future, it is recommended that viscous effects be incorporated in this model.

The sigma-transformation is limited to unique stretchings of continuous liquid between the free surface and bed in the vertical direction. This limitation could be overcome to a certain extent by the use of boundary-fitted curvilinear systems (see e.g. Mayer *et al.* [27]). Curvilinear mappings enable submerged bodies to be inserted in the liquid domain (Thompson *et al.* [28]), and could be the subject of further investigation using the spectral collocation method.

ACKNOWLEDGMENTS

This research has been supported by the Government of Taiwan, the British Overseas Research Student (ORS) Awards Scheme and a Wei-Lun graduate scholarship from St. Hugh's College, Oxford. Substantial computational resources have been provided by the Oxford Supercomputing Centre (OSC). The authors are also grateful to Dr Q.W. Ma and Dr G.X. Wu of University College London who provided their numerical results for comparison.

APPENDIX A. NOMENCLATURE

a	initial wave elevation amplitude
b	distance between inner cylinder and cylindrical tank wall, $r_O - r_I$
B_k	Bessel coefficient
c	wave phase speed
d	still water depth
f	function integrated by Adams–Bashforth scheme
F_x, F_y	horizontal wave force components acting on the inner cylinder
g	acceleration due to gravity
$\hat{\boldsymbol{GR}}^{(q)}$, $\hat{\boldsymbol{G\theta}}^{(q)}$, $\hat{\boldsymbol{GZ}}^{(q)}$	matrix to evaluate the qth derivatives with respect to R, θ and σ
h	local water depth, a function of r, θ and time, t
J_0, J_1	Bessel functions of the first kind of order 0 and 1 respectively
M, N, L	number of collocation points
p	pressure
q	geometric variable, $q = b(R+1) + 2r_I$
R	stretched radial co-ordinates in the computational domain
r_O	outer radius of the cylindrical tank
r_I	radius of inner cylinder at tank centre
r, θ, z	radial, angular and vertical co-ordinates in the physical domain
t	time
t^*	non-dimensional time, $t^* = t(g/d)^{1/2}$
u_r, u_θ, u_z	velocity components in cylindrical co-ordinate system
Y_0, Y_1	Bessel functions of the second kind of order 0 and 1 respectively
Z_k	combined Bessel function, $Z_k(r) = J_o(\alpha_k r) + B_k Y_0(\alpha_k r)$

Greek letters

α, β, γ	sigma-transformation parameters
α_k	Bessel coefficient
ϕ	velocity potential, $\phi(r, \theta, z, t)$
ϕ_1	first-order solution for velocity potential
ϕ_2	second-order solution for velocity potential
η	free surface elevation above still water level
η_1	first-order solution for free surface elevation
η_2	second-order solution for free surface elevation, $\eta_2 = \eta_2^{(1)} + \eta_2^{(2)}$
$\eta_2^{(1)}$	first component of second-order solution for free surface elevation
$\eta_2^{(2)}$	second component of second-order solution for free surface elevation
ρ	water density
σ	sigma-transformation variable that replaces z
ω_k	angular wave frequency
Φ	velocity potential, $\Phi(R, \theta, \sigma, t)$
∇	gradient operator

Subscripts

i, j, k	spatial indices

Superscript

n	temporal index

REFERENCES

1. Rozario JB, Tromans PS, Taylor PH, Efthymiou M. Comparison of loads predicted using 'newwave' and other wave models with measurements on the Tern structure. *Wave Kinematics and Environmental Forces (Society for Underwater Technology)* 1993; **29**: 143–159.
2. Stokes GG. On the theory of oscillatory waves. *Transactions of Cambridge Philosophy Society* 1847; **8**: 441–455.
3. Schwarz LW. Computer extension and analytic continuation of Stokes' expansion for gravity waves. *Journal of Fluid Mechanics* 1974; **62**: 535–578.
4. Fenton JD. A fifth order Stokes' theory for steady waves. *ASCE Journal of Waterways*, *Port*, *Coastal and Ocean Engineering* 1985; **111**: 216–234.
5. Malenica S, Molin B. Third harmonic wave diffraction by a vertical cylinder. *Journal of Fluid Mechanics* 1995; **302**: 203–229.
6. Ma QW, Wu GX. Second order transient waves around a vertical cylinder in a tank. *Journal of Hydrodynamics Series* 1995; **B4**: 72–81.
7. Yeung RW. Numerical methods in free-surface flows. *Annual Review of Fluid Mechanics* 1982; **14**: 395–442.
8. Dold JW, Peregrine DH. An efficient boundary-integral method for steep unsteady water waves. In *Numerical Methods for Fluid Dynamics II*, Morton KW, Baines MJ (eds). Oxford University Press: Oxford, 1986; 671–691.
9. Wang P, Yao Y, Tulin MP. An efficient numerical tank for non-linear waves, based on the multi-subdomain approach with BEM. *International Journal for Numerical Methods in Fluids* 1995; **20**: 1315–1336.
10. Ferrant P. Simulation of strongly non-linear wave generation and wave-body interacting using a 3D MEL model. In *Proceedings of 21st ONR Symposium on Naval Hydrodynamics*, Trondheim, Norway. National Academy Press: Washington DC, 1996.
11. Taylor PH, Haagsma IJ. Focusing of steep wave groups on deep water. In *Proceedings of International Symposium for Waves-Physical and Numerical Modelling*, Isaacson M, Quick (eds). Department of Civil Engineering, University of British Columbia: Vancouver, B.C., 1994; 862–870.
12. Johannessen TB. The effect of directionality on the nonlinear behaviour of extreme transient ocean waves. PhD thesis, Imperial College, London, 1997.
13. Fenton JD. Polynomial approximations and water waves. *Proceedings of 20th International Conference on Coastal Engineering* 1986; **1**: 193–207.
14. Forristal GZ. Irregular wave kinematics from a kinematic boundary condition fit. *Applied Ocean Research* 1985; **7**: 202–212.
15. Yeung RW, Vaidhanathan M. Nonlinear wave diffraction over submerged obstacles. In *Proceedings of 5th International Workshop on Water Waves and Floating Bodies*, Martin PA (ed.). University of Manchester: Manchester, 1990; 208–212.
16. Wu GX, Eatock Taylor R. Finite element analysis of two-dimensional non-linear transient water waves. *Applied Ocean Research* 1994; **16**: 363–372.
17. Yu X, Yeung RW. Interaction of transient waves with a circular surface-piercing body. *Journal of Fluids Engineering-Transactions of the ASME* 1995; **117**: 382–388.
18. Gottlieb D, Orszag SA. *Numerical Analysis of Spectral Methods: Theory and Applications*. Society for Industrial and Applied Mathematics: Philadelphia, PA, 1977.
19. Hussaini MY, Zang TA. Spectral methods in fluid dynamics. *Annual Review of Fluid Mechanics* 1987; **19**: 339–367.
20. Canuto C, Hussaini MY, Quarteroni A, Zang TA. *Spectral Methods in Fluid Dynamics*. Springer-Verlag: Berlin, 1988.
21. Chern MJ, Borthwick AGL, Eatock Taylor R. A pseudospectral sigma-transformation model of two-dimensional nonlinear waves. *Journal of Fluids and Structures* 1999; **13**: 607–630.
22. Orlanski I. A simple boundary condition for unbounded hyperbolic flows. *Journal of Computational Physics* 1976; **21**: 251–269.

23. Chan RK-C. Finite difference simulations of the planar motion of a ship. In *Proceedings of 2nd International Conference on Numerical Ship Hydrodynamics*, Wehausen JV, Salvesen N (eds). University Extension Publications, University of California: Berkeley, CA, 1977; 39–56.
24. Romate JE. Absorbing boundary conditions for free surface waves. *Journal of Computational Physics* 1992; **99**: 135–145.
25. Broeze J, Romate JE. Absorbing boundary conditions for free surface wave simulations with a panel method. *Journal of Computational Physics* 1992; **99**: 146–158.
26. Longuet-Higgins MS, Cokelet ED. The deformation of steep surface waves on water I. A numerical method of computation. *Proceedings of Royal Society (London)* 1976; **A350**: 1–26.
27. Mayer S, Garapon A, Sorenson L. Finite volume solutions to unsteady free surface flow with application to gravity waves. In *Coastal Dynamics '97*, Plymouth, Thornton EB (ed.). American Society of Civil Engineers: Reston, VA, 1997; 118–127.
28. Thompson JF, Sonu BK, Weatherill NP (eds). *Handbook of Grid Generation*. CRC Press: Boca Raton, FL, 1999.

